Analytica Chimica Acta 1140 (2020) 78–88

Contents lists available at ScienceDirect

Analytica Chimica Acta

journal homepage: www.elsevier.com/locate/aca

An efficient electrochemical assay for miR-3675-3p in human serum based on the nanohybrid of functionalized fullerene and metal-organic framework

Jianli Zuo [a, 1], Yonghua Yuan [a, 1], Min Zhao [b], Jie Wang [a], Yuhan Chen [c], Qiqi Zhu [a], Lijuan Bai [a, *]

[a] Chongqing Research Center for Pharmaceutical Engineering, College of Pharmacy, Chongqing Medical University, Chongqing, 400016, PR China
[b] Key Laboratory of Clinical Laboratory Diagnostics (Ministry of Education), College of Laboratory Medicine, Chongqing Medical University, Chongqing, 400016, PR China
[c] Department of Respiratory and Critical Care Medicine, the First Affiliated Hospital of Chongqing Medical University, Chongqing, 400016, PR China

HIGHLIGHTS

- C_{60}@PAMAM-MOF was first synthesized and applied as redox nanoprobe and nanocarrier to generate and amplify detection signal.
- Au@PtNPs decorated CS-AB as sensing platform further accelerated electron transfer and enhanced the response signal.
- The proposed microRNA biosensor showed wider linear range and lower detection limit compared with that of qRT-PCR.
- This method exhibited satisfactory results for miR-3675-3p detection in serum samples.

GRAPHICAL ABSTRACT

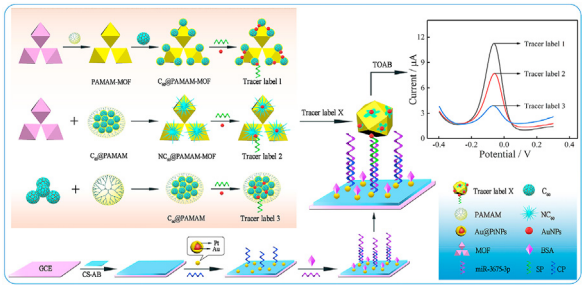

ARTICLE INFO

Article history:
Received 11 June 2020
Received in revised form
2 October 2020
Accepted 10 October 2020
Available online 14 October 2020

Keywords:
Idiopathic pulmonary fibrosis
Novel redox nanoprobe
Functionalized nanohybrid
Multiple signal amplification

ABSTRACT

Idiopathic pulmonary fibrosis (IPF) is an interstitial lung disease with unclear pathogenesis, for which diagnosis has been a great challenge. Recent researches have revealed that miR-3675-3p is a promising biomarker for IPF diagnosis. Herein, the present work describes a novel electrochemical microRNA biosensor for rapid and sensitive detection of miR-3675-3p based on multiple signal amplification strategies. First of all, fullerene (C_{60}) is doped with poly(amidoamine) (PAMAM)-functionalized metal-organic framework (MOF) to form a new nanohybrid of C_{60}@PAMAM-MOF, which exhibits more remarkable redox activity compared with the other two synthesized C_{60}-based nanohybrids when triggered by tetraoctylammonium bromide (TOAB). C_{60}@PAMAM-MOF also possesses a large specific surface area and abundant amino groups to anchor Au nanoparticles (AuNPs) for the immobilization of signal probe (SP) to form tracer label and enhance the electrochemical response signal. In addition, core@shell Au–Pt nanoparticles (Au@PtNPs) are absorbed on chitosan-acetylene black (CS-AB) to act as sensing platform, which can promote electron transfer and increase the loading of capture probe (CP). Under optimum conditions, the proposed biosensor displays a wide linear range for miR-3675-3p from 10 fM to 10 nM, with a limit of detection (LOD) as low as 2.99 fM. More significantly, this biosensor shows

* Corresponding author.
E-mail address: bailj1018@cqmu.edu.cn (L. Bai).
[1] Jianli Zuo and Yonghua Yuan contributed equally to this work.

https://doi.org/10.1016/j.aca.2020.10.017

a lower LOD and wider linear range than that of qRT-PCR, and its trial application in human serum shows favorable results, which exhibits a promising prospect for IPF diagnosis.

1. Introduction

Idiopathic pulmonary fibrosis (IPF) is a severe chronic and progressive interstitial lung disease caused by fibroblast proliferation, epithelial injury and extracellular matrix deposition [1]. Up to now, IPF has afflicted 3 million people and held median survival of 2–3 years, and the incidence and mortality are gradually increasing [2]. The clinical symptoms, dyspnea and dry cough, are unrepresentative and prone to be ignored, so cautious screening of the patients with these symptoms is crucial to timely detection of IPF. At present, high-resolution computed tomography (HRCT) with the advantages of non-invasive and highly sensitive is extensively used in the diagnosis of IPF. However, not all patients have typical HRCT features (approximately 30% of patients present indeterminate HRCT patterns) and require further diagnostic examinations. According to the guidelines of *Diagnosis of Idiopathic Pulmonary Fibrosis* in 2018, surgical lung biopsy (SLB) and a multiple disciplinary team are recommended for the diagnosis of these patients [3,4]. SLB was also recommended especially in the patients with pattern of unconfident HRCT diagnosis and probable interstitial lung disease, but its application is restricted by the cost and invasiveness [5]. Therefore, it is urgent to develop a non-invasive diagnostic procedure, such as a biomarker detector, to assist the diagnosis of IPF.

MicroRNA (miRNA), a group of noncoding short-sequence single-strand RNA (approximately 22 nucleotides in length), is the most common serum biomarker for diagnosis. It has been shown that aberrant expression of miRNA plays a pivotal role in IPF [6]. It is reported that miR-3675-3p can be a suitable candidate-specific biomarker for IPF diagnosis [7] for it is significantly overexpressed in IPF patients in comparison to healthy control group [8]. To date, conventional methods for miRNA detection include quantitative real-time polymerase chain reaction (qRT-PCR), northern blotting and microarray [9]. Detection of miRNA using qRT-PCR exhibits high sensitivity but requires professional skills, specialized equipment and is prone to false-positive results. Northern blotting and microarray are limited by low efficiency, expensive cost and lengthy detection time. Therefore, it is necessary to develop a sensitive, cost-effective and fast alternative. Of late, the electrochemical biosensor is extensively applied due to high sensitivity and portability. However, electrochemical assay alone is unfit for quantification of miRNA owing to small molecular size, low abundance and similar sequence. To solve this defect, a signal amplification strategy based on nanomaterials is introduced to enhance the sensitivity of the electrochemical biosensor.

Metal-organic framework (MOF), an emerging porous nanomaterial, is composed of metal ions/clusters and organic linkers via coordination bonds [10]. Recently, MOF has attracted great attention because of large surface area, high porosity, controllable size and easy functionalization, and has been widely applied in various fields such as sensors [11], catalysts [12], gas storage [13], drug delivery [14] and so forth. It is well known that MOF in combination with carbon nanomaterials remarkably improves the detection performance of a biosensor. For example, Fu et al. prepared NH_2-MIL-101(Fe)-graphene oxide via Fe–O covalent bond, which enhanced electrical conductivity and stability for simultaneous detection of uric acid, xanthine and hypoxanthine [15]. Cai et al. synthesized flake-like Mn-MOF-single walled carbon nanotubes (Mn-MOF-SWCNTs) for Pb^{2+} detection with favorable anti-interference performance [16]. Hatamluyi et al. used carbon quantum dots decorated by hexagonal boron nitride (CQDs@HBN) and UiO-66-NH_2 self-assembly modified on the electrodes for improved sensitivity to detect oxaliplatin [17]. In short, the performance improvement of the aforementioned biosensors is mainly attributed to the synergistic effect among MOF and carbon materials, and it is reasonable to hypothesize that MOF in combination with other carbon materials will also display the similar synergistic effect and outstanding electrochemical performance.

Fullerene (C_{60}), a common zero-dimensional carbon material, has the advantages of high conductivity, strong electron receptivity and large specific surface area [18–20]. Besides, it possesses unique redox activity compared with other carbon allotropes, and is considered as an ideal electrical signal material and redox nanoprobe. In our previous work, we successfully synthesized C_{60}-doped polyaniline (C_{60}-PAn) [21] and C_{60}NPs-decorated N-CNTs/GO (C_{60}NPs-N-CNTs/GO) [22] as redox nanoprobes to construct aptasensors for ultrasensitive detection of MPT64 antigen. To the best of our knowledge, designing the nanohybrid of MOF coupled with C_{60} as redox nanoprobe in electrochemical biosensors has not been reported.

Based on the above description, we successfully synthesized two new nanohybrids via two facile methods, which were labeled as C_{60} doped poly(amidoamine)-MOF (C_{60}@PAMAM-MOF) and needle-like C_{60} doped poly(amidoamine) conjugated with MOF (NC_{60}@PAMAM-MOF), respectively. These nanocomposites not only revealed that large specific surface area to adsorb plenty of biomolecules, but also exhibited prominent redox activity and favorable electrical conductivity [23]. More importantly, both the two nanohybrids exhibited outstanding electrochemical performance in comparison to C_{60} doped poly(amidoamine) (C_{60}@PAMAM), and C_{60}@PAMAM-MOF showed a superior electrochemical signal and was selected as the signal amplifier for application in whole experiment.

Acetylene black (AB), another carbon material with prominent electrical conductivity and adsorption capacity, is a favorable substrate material and has been extensively applied in electrochemical biosensor. For example, Ibrahim and Shuai's groups successfully prepared AB-CeO_2NPs [24] and tungsten disulfide/AB (WS_2-AB) [25] nanocomposites which exhibited outstanding conductivity and used them as sensor platform to improve sensitivity of the biosensor. Additionally, bimetallic nanoparticles with core@shell structure, such as bimetallic Au@Pt nanoparticles (Au@PtNPs), were also widely applied owing to larger specific surface area and higher conductivity than monometallic [26].

Herein, a facile electrochemical miRNA biosensor for miR-3675-3p determination was constructed using Au@PtNPs decorated chitosan-AB (CS-AB) as sensing platform and C_{60}@PAMAM-MOF as signal amplifier for the first time. First of all, CS-AB was modified onto the surface of glassy carbon electrode (GCE) to increase the conductivity and specific surface area of GCE. Then abundant Au@PtNPs were assembled on CS-AB for the immobilization of thiol-modified capture probe (CP) via Pt–S bonds. Meanwhile, the newly designed C_{60}@PAMAM-MOF nanohybrid was decorated with AuNPs to attach the signal probe (SP) to form the tracer label. After

the hybridization among CP, miR-3675-3p and SP, quantitative detection of miR-3675-3p was realized with the redox activity of tracer label motivated by tetraoctylammonium bromide (TOAB). The stepwise fabrication procedure of the miRNA biosensor and comparison of different tracer labels were illustrated in Fig. 1.

2. Experimental section

2.1. Materials and chemicals

Fullerene (C_{60}, 99.5%) powder and acetylene black (AB, electronic grade) were purchased from XianFeng Nano Materials (Nanjing, China) and Aiweixin Chemical (Tianjin, China) Technology Co., Ltd, respectively. Amine-terminated poly(amidoamine) (PAMAM, G5.0), chloroauric acid ($HAuCl_4$), chloroplatinic acid (H_2PtCl_6) and 2-aminoterephthalic acid (99%) were ordered from Sigma-aldrich (USA). Tetraoctylammonium bromide (TOAB, 98%) and bovine serum albumin (BSA, 98%) were obtained from Yuanye Biotechnology (Shanghai, China) and Bailingwei Technology (Beijing, China) Co., Ltd. Tris (2-carboxyethyl) phosphine hydrochloride (TCEP, 98%) and iron (III) chloride hexahydrate ($FeCl_3 \cdot 6H_2O$, 99%) were purchased from Aladdin (USA). Chitosan (CS), ascorbic acid (AA), sodium borohydride ($NaBH_4$) and trisodium citrate dihydrate were ordered from Chengdu Kelong Chemical Reagent (Chengdu, China). N, N-Dimethylformamide (DMF) and toluene were obtained from Macklin Biochemical (Shanghai, China) and Chuandong Chemical (Chongqing, China) Co., Ltd, respectively. FastStart Universal SYBR Green Master (Rox) was obtained from Servicebio technology Co., Ltd (Wuhan, China). RevertAid First Strand cDNA Synthesis Kit was ordered from Thermo Scientific (USA). Other chemicals were of analytical purity. Ultrapure water (with resistivity of 18.2 MΩ cm) was employed in the whole experiment. Diethyl pyrocarbonate (DEPC) water and the nucleotides were provided by Sangon Biotech Co., Ltd (Shanghai, China), and all the nucleotides were purified by HPLC. Sequences of the nucleotides are summarized in Table 1.

All miRNAs were dissolved in DEPC water and stored in an RNase-free tube at −80 °C to avoid degradation. The DNAs were dissolved in the TES buffer solution containing 0.1 M NaCl, 1 mM EDTA and 10 mM TCEP and stored at −20 °C.

2.2. Instruments and measurement

The images of scanning electron microscope (SEM) and energy dispersive spectroscopy (EDS) were recorded with field emission-scanning electron microscope instrument (Merlin Compact, Germany) at 10.0 kV. Transmission electron microscopy (TEM) images were collected with Talos F200X instrument (Thermo Fischer, USA). Fourier transform-infrared (FT-IR) and UV–vis absorption spectrum were collected with Nicolet iS50 (Thermo Fisher, USA) and UV-2600 spectrophotometer (Kyoto, Japan). qRT-PCR was performed with Stepone plus (ABI, USA), and RNA concentration was measured with NanoDrop 2000 spectrophotometer (Thermo Scientific, USA). The electrochemical procedure was performed with CHI660E electrochemical workstations (Shanghai, China) using the classical three-electrode system which included the reference electrode (saturated calomel electrode, SCE), the auxiliary electrode (platinum wire) and the working electrodes (GCE). The measurement methods included differential pulse voltammetry (DPV), cyclic voltammetry (CV) and electrochemical impedance spectroscopy (EIS). The DPV experiments were measured in 0.1 M PBS solution (containing 10 mM KCl and 2 mM $MgCl_2$), which were performed from −0.4 V to 0.3 V (with a scan rate of 20 mV s^{-1}, a potential step of 4 mV, an amplitude of 50 mV and a pulse width of 50 ms). The CV experiments were performed in 5 mM $[Fe(CN)_6]^{3-/4-}$ containing 0.1 M KCl from −0.2 V to 0.6 V with a scan rate of 100 mV s^{-1} for 6 cycles. The EIS measurements were performed in $[Fe(CN)_6]^{3-/4-}$ containing 0.1 M KCl at frequencies ranging from 0.1 Hz to 0.1 MHz (with an amplitude of 50 mV and quiet time of 2 s).

2.3. Preparation of MOF

MOF was synthesized with the solvothermal method based on previously reports with slight improvements [27]. Typically, 15 mL of DMF containing 0.187 g of $FeCl_3 \cdot 6H_2O$ (0.692 mmol) and 0.126 g of 2-aminoterephthalic acid (0.692 mmol) were transferred to the vial, and 207 μL of acetic acid (3.45 mmol) was added into it. Then,

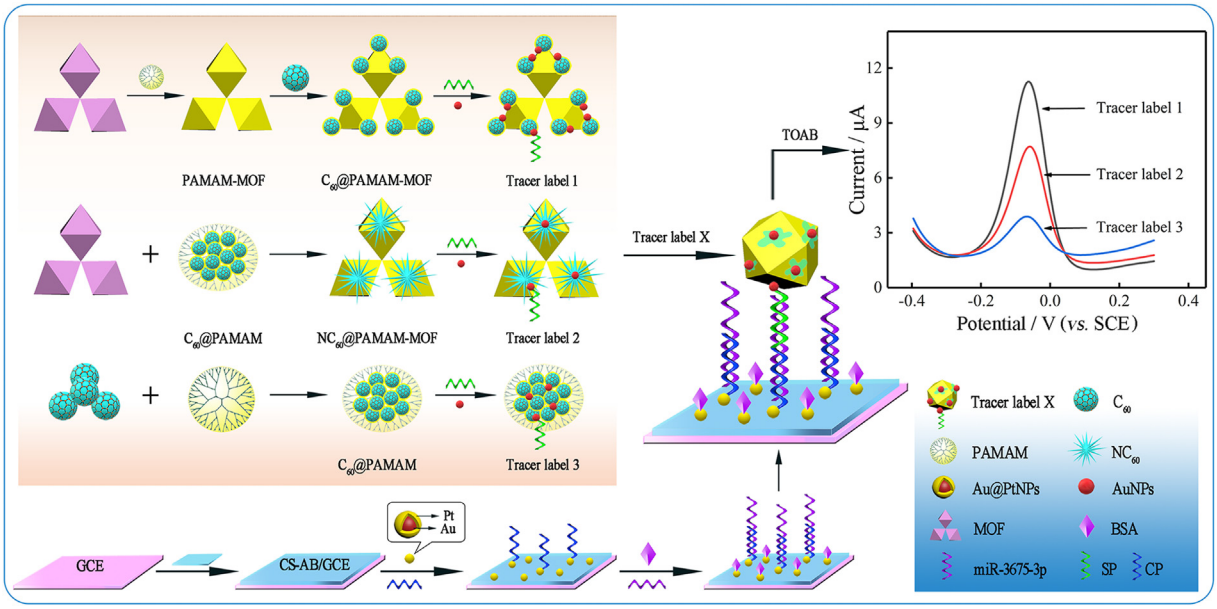

Fig. 1. Schematic diagrams of the preparation process of three tracer labels and the construction of the electrochemical miRNA biosensor for detection of miR-3675-3p.

Table 1
List of the oligonucleotide sequences employed in this work.

Nucleotide name	Nucleotide sequence (5'→3')
miR-3675-3p (Target)	CAUCUCUAAGGAACUCCCCCAA
Capture Probe (CP)	CCTTAGAGATG-$(CH_2)_6$-SH
Signal Probe (SP)	SH-$(CH_2)_6$-TTGGGGGAGTT
Let-7d-5p	AGAGGUAGUAGGUUGCAUAGUU
Single base mismatch (SBM)[a]	CAUCUCUAAGGAACUC**A**CCCAA
Forward primer	ACACTCCAGCTGGGCATCTCTAAGGAACT
Downstream primer	TGGTGTCGTGGAGTCG
Reverse primer	CTCAACTGGTGTCGTGGAGTCGGCAATTCAGTTGAG TTGGGGAG

[a] The underlined part of the sequence represented the mismatch site of the target miRNA.

the mixture was moved to the oil bath and stirred for 4 h at 120 °C. When cooled to room temperature, the brown-red solution was sequentially washed with DMF and ethanol (10000 rpm, 8 min) to remove excrescent impurities and dried to obtain MOF.

2.4. Preparation of C_{60}@PAMAM-MOF, NC_{60}@PAMAM-MOF and C_{60}@PAMAM

The nanohybrid of C_{60}@PAMAM-MOF was prepared with the phase-transfer method. Briefly, 5 mg of MOF was dissolved in 5 mL of ultrapure water, resulting in a brown-red solution, and after addition of 200 μL of PAMAM, the brown-red color changed into bright-yellow. After stirring overnight, the product was washed by ultrapure water for several times and was re-dispersed in 5 mL of ultrapure water to obtain PAMAM-MOF, and then 20 mL of ethanol was added. Next, the mixture was added into 5 mL of toluene-soluble C_{60} (1 mg mL^{-1}) with magnetic stirring for 30 h at room temperature. The resultant mixture was subjected to centrifugation, and the sediment was washed successively with ethanol and ultrapure water, and dispersed into 5 mL of ultrapure water to gain C_{60}@PAMAM-MOF (1 mg mL^{-1}) and stored at 4 °C in a refrigerator.

For comparison, C_{60}@PAMAM (1 mg mL^{-1}) was prepared following the same steps in the absence of MOF, and NC_{60}@PAMAM-MOF was prepared via a direct-mixing method with the same substrates. To prepare NC_{60}@PAMAM-MOF, 5 mL of MOF (1 mg mL^{-1}) was added into 5 mL of C_{60}@PAMAM with stirring for 30 h. The excess reactant was removed by centrifugation, and the product was washed with ultrapure water for several times and dispersed in ultrapure water to obtain NC_{60}@PAMAM-MOF (1 mg mL^{-1}).

2.5. Preparation of the three tracer labels

AuNPs were loaded on the surface of C_{60}@PAMAM-MOF by reduction of $HAuCl_4$ with $NaBH_4$. Concretely, 1 mL of $HAuCl_4$ (1%) was put into 5 mL of C_{60}@PAMAM-MOF with stirring for 15 min and followed by addition 2 mL of $NaBH_4$ (4 mg mL^{-1}) for 40 min, in which process AuNPs were immobilized via Au—N bonds to obtain C_{60}@PAMAM-MOF-AuNPs. After that, the signal probe (SP, 2 μM) was pretreated with TES buffer containing 10 mM TCEP and then added to the mixture at 4 °C and kept for 12 h to obtain C_{60}@PAMAM-MOF-AuNPs-SP (Tracer label 1). Analogously, NC_{60}@PAMAM-MOF-AuNPs-SP (Tracer label 2) and C_{60}@PAMAM-AuNPs-SP (Tracer label 3) were prepared likewise.

2.6. Preparation of CS-AB and core@shell Au@PtNPs

CS-AB suspension was prepared on the basis of a reported method [28]. 1 mg of AB was dispersed in chitosan-acetic acid solution (0.5 wt%) with ultrasound treatment to obtain a suspension of CS-AB. Core@shell Au@PtNPs were synthetized by the reduction method according to our previous work [29]. In the first step, 2.5 mL of trisodium citrate was put into 100 mL of boiled $HAuCl_4$ solution for 15 min. When the mixture was cooled to room temperature, the color changed from blue to claret, and colloidal AuNPs was successfully synthesized. In the next step, 20 mL of colloidal AuNPs was added in 30 mL of ultrapure water and was heated to 80 °C. Then 2.5 mL of H_2PtCl_6 was quickly poured and 1.75 mL AA was slowly dripped into the mixture respectively, and the mixture was heated until the color turned black and remained so. The obtained Au@PtNPs were transferred to a brown bottle and stored at 4 °C for future use.

2.7. Fabrication of the electrochemical miRNA biosensor

GCE (Φ = 4 mm) was polished with alumina powder (0.3 and 0.05 μm) and sonicated in ultrapure water and ethanol several times prior to use. Firstly, 6 μL of CS-AB suspension and 6 μL of Au@PtNPs were successively dripped onto the mirror-like GCE and naturally dried in the air. Then 20 μL of CP (2 μM) containing 10 mM TCEP was thrown onto the electrode surface and kept at room temperature for 12 h, and the electrode was incubated with 20 μL BSA (0.25 wt%) blocked the non-specific sites for 45 min and then cleaned with ultrapure water. Next, 20 μL of target miR-3675-3p in various concentrations and 20 μL of as-prepared Tracer label 1 were dropped onto the surface and each hybridized at 37 °C for 2 h, and then the electrode was rinsed with DEPC water to remove non-hybridized nucleic acid. Finally, 10 mM TOAB was pipetted onto the modified electrode to provoke the intrinsic redox activity of Tracer label 1, and the electroactivity was recorded in DPV.

3. Results and discussion

3.1. Morphological and elemental characterization of different nanocomposites

The morphology of the as-prepared nanocomposites was characterized by SEM. Pure MOF (Fig. 2A) displayed regular octahedral structures in accordance with previous report [30]. The dispersive octahedrons were aggregated with the addition of PAMAM due to physical absorption of PAMAM on the MOF surface (Fig. 2B). After doping with C_{60} (Fig. 2C), the irregular spheres with different diameters tightly connected with PAMAM-MOF through the amino groups reacted with C_{60}, exhibiting large specific surface area [31]. Simultaneously, TEM mapping (Fig. 2F) displayed uniform distribution of C (red), Fe (yellow), O (blue) and N (green) elements in C_{60}@PAMAM-MOF. These results indicated the successful preparation of C_{60}@PAMAM-MOF. As shown in Fig. 2D, a large number of shining AuNPs could be found on the surface of C_{60}@PAMAM-MOF, and the existence of Au elements was corroborated with EDS (Fig. 2E).

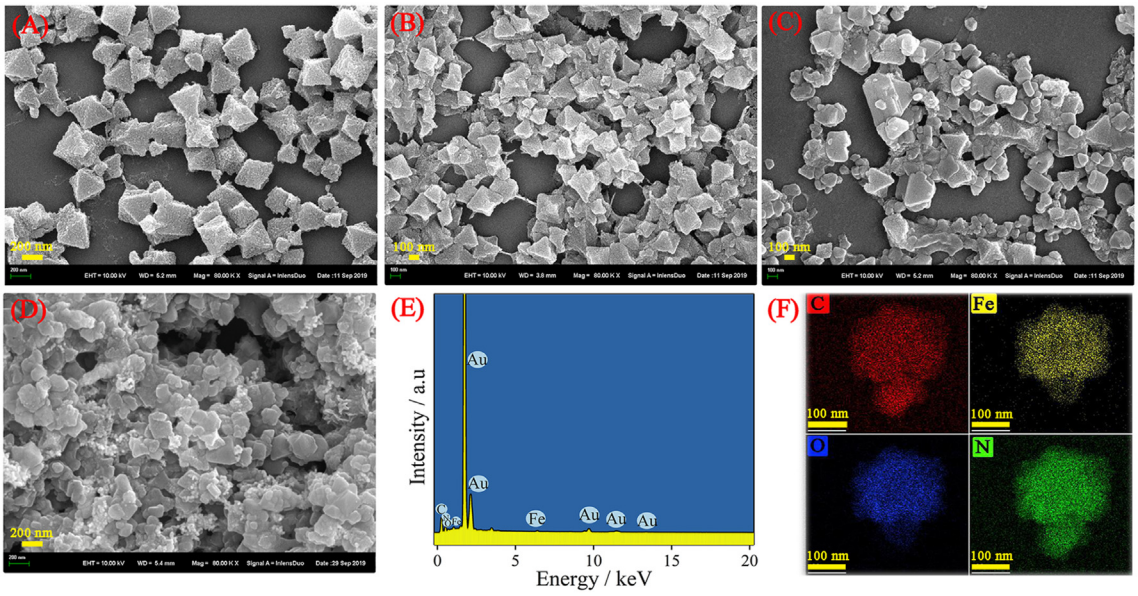

Fig. 2. The SEM images of (A) MOF, (B) PAMAM-MOF, (C) C_{60}@PAMAM-MOF, (D) C_{60}@PAMAM-MOF-AuNPs. (E) The EDS images of C_{60}@PAMAM-MOF-AuNPs. (F) The TEM element mapping images of C_{60}@PAMAM-MOF.

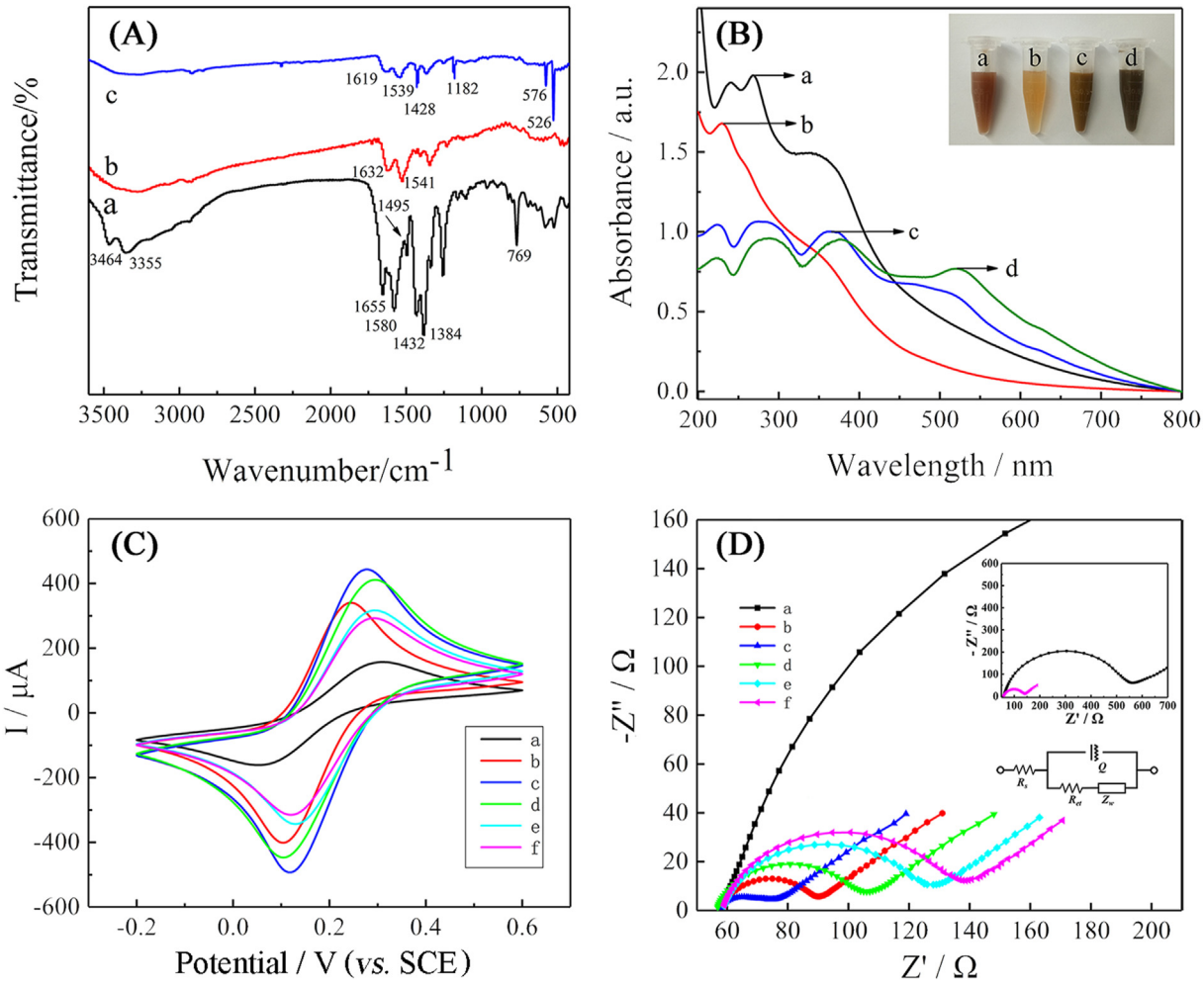

Fig. 3. (A) FT-IR spectra of (a) MOF, (b) PAMAM-MOF and (c) C_{60}@PAMAM-MOF. (B) UV–vis spectra of (a) MOF, (b) PAMAM-MOF, (c) C_{60}@PAMAM-MOF and (d) C_{60}@PAMAM-MOF-AuNPs. (C) CV and (D) EIS of characterization step by step of various electrodes in 5 mM $[Fe(CN)_6]^{3-/4-}$ containing 0.1 M KCl: (a) bare GCE, (b) CS-AB/GCE, (c) Au@PtNPs/CS-AB/GCE, (d) CP/Au@PtNPs/CS-AB/GCE, (e) BSA/CP/Au@PtNPs/CS-AB/GCE and (f) miR-3675-3p/BSA/CP/Au@PtNPs/CS-AB/GCE.

3.2. Structural characterization of different nanocomposites

FT-IR spectrum was used to verify the structure of the nanomaterials, and the results were shown in Fig. 3A. Curve a showed the characteristic bands of MOF in accordance with other previous reports [32–34]. Concretely, the 3464 cm^{-1} and the 3355 cm^{-1} bands were attributed to the symmetrical and asymmetric vibrations of the terminal amino groups [32], and the 1655–1384 cm^{-1} bands were mainly derived from carboxylate [33]. The 769 cm^{-1} band illustrated the formation of Fe–O, which indicated the successful synthesis of MOF [34]. After modification with PAMAM, a great deal of characteristic peaks of MOF vanished and the remaining two peaks shifted to 1632 and 1541 cm^{-1}, which proved that PAMAM-MOF was successfully synthesized [35,36]. After doping with C_{60}, the bands of PAMAM-MOF displayed a slight blue-shift and exhibited four new peaks (1428, 1182, 576 and 526 cm^{-1}) on curve c, which confirmed the formation of C_{60}@PAMAM-MOF [22].

Simultaneously, synthesis of nanomaterials was also confirmed with UV–vis absorption spectrum. As shown in Fig. 3B, MOF (curve a) exhibited three characteristic peaks at 240, 268 and 338 nm [37]. After functionalization with PAMAM, the peak of PAMAM-MOF (curve b) was shown at 229 nm, which was attributed to the strong absorption peak of PAMAM because the characteristic peaks of pure PAMAM were approximately at 230 and 283 nm [38]. C_{60}@PAMAM-MOF (curve c) showed three strong absorption peaks at 224, 275 and 363 nm, which indicated the formation of C_{60}@PAMAM-MOF. The wide absorption peak was attributed to $C_{60} \rightarrow C_{60}^{+}$ and the peak at 363 nm was attributed to π-π* electronic transition [39,40]. After the modification with AuNPs (curve d), the characteristic peak of AuNPs at 520 nm can be clearly observed, which was mainly the result of surface plasmon resonance [41]. Meanwhile, the changed in color also proved the successful synthesis of the nanomaterials (see in the inset).

3.3. Electrochemical characterization of the miRNA biosensor

The stepwise fabrication of the biosensor and the electron transfer of the interface was monitored with CV and EIS. The CV plot exhibited redox behavior of the as-prepared biosensor in 5 mM $[Fe(CN)_6]^{3-/4-}$ solution containing 0.1 M KCl. As shown in Fig. 3C, the bare GCE (curve a) displayed a couple of reduction and oxidation peaks, which was attributed to the redox reaction of $K_3[Fe(CN)_6]$ and $K_4[Fe(CN)_6]$ ($[Fe(CN)_6]^{3-} + e^- \leftrightarrow [Fe(CN)_6]^{4-}$) [42,43]. After modification with CS-AB (curve b) and Au@PtNPs (curve c), the peak current evidently increased because of the outstanding

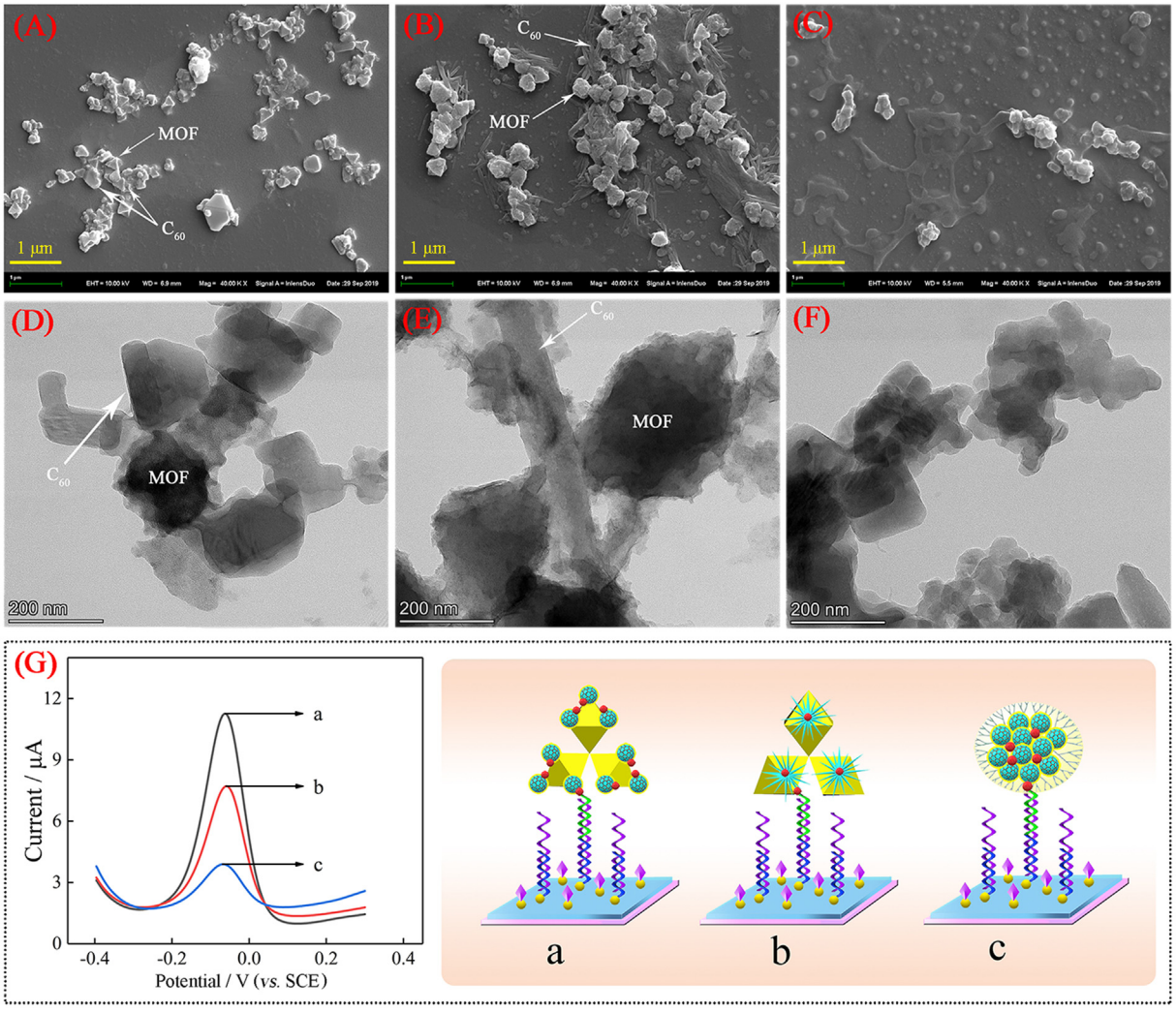

Fig. 4. The SEM and TEM images of C_{60}@PAMAM-MOF (A and D), NC_{60}@PAMAM-MOF (B and E), C_{60}@PAMAM (C and F). (G) Three tracer labels were characterized in 0.1 M PBS and three biosensors were shown in the right picture.

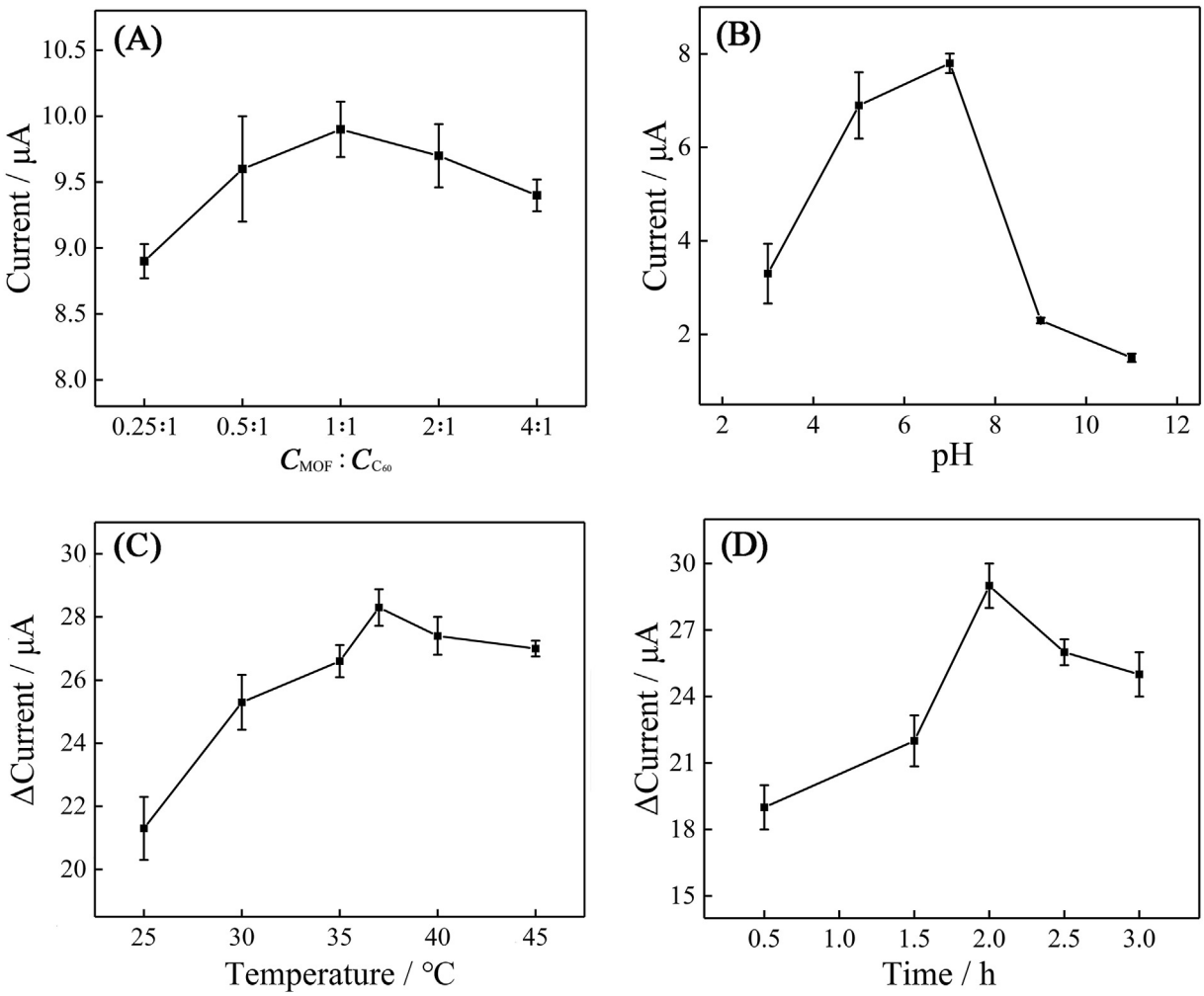

Fig. 5. Effect of (A) concentration ratio of MOF:C_{60} and (B) pH in 0.1 M PBS. Effect of (C) hybridization temperature and (D) hybridization time in the 5 mM $[Fe(CN)_6]^{3-/4-}$ containing 0.1 M KCl. Error bars represent the standard deviation (n = 3).

conductivity of AB and the bimetallic synergistic conduction effect of Au@Pt. In contrast, the capture probe (curve d) was immobilized and the peak current reduced due to the repulsive interaction between the negative charge of DNA and $[Fe(CN)_6]^{3-/4-}$. Subsequently, non-conductive BSA (curve e) was applied to block non-specific binding sites and hindered the electron transfer, resulting in the decrease of peak current. Finally, miR-3675-3p (curve f) was hybridized and caused the peak current decreased again.

EIS is used to further verify the electronic transmission efficiency of the interface and plotted as Nyquist diagram (Z': real impedance; Z'': imaginary impedance). As showed in Fig. 3D, the straight line expressed the diffusion-limited process in the solution and the diameter of semicircle represented the electron transfer resistance (Ret). The semicircular diameter sharply reduced after immobilization of CS-AB (curve b) and Au@PtNPs (curve c), compared with bare GCE (curve a), owing to accelerated electron transfer with the large surface area. The increase of the semicircular diameter indicated successful assemble of the capture probe (curve d) and BSA (curve e) onto the modified electrode and the consequently impeded electron transfer. When miR-3675-3p (curve f) was hybridized with DNA, the semicircular diameter increased again owing to the formation of double strands that make electron transport slower and steric hindrance larger. In addition, the equivalent circuit (inset, Fig. 3D) was obtained by fitting the EIS data with ZSimDemo software, which consisted of electrolyte resistance (R_s), constant phase element (Q), electron transfer resistance (R_{et}) and Warburg impedance (Z_w) [42]. The fitting values of these parameters were illustrated in Table S1 (see in Supplementary Material).

3.4. Comparison of the three tracer labels

To investigate the signal amplification of C_{60}@PAMAM-MOF, NC_{60}@PAMAM-MOF and C_{60}@PAMAM were successfully prepared as controls and characterized by SEM and TEM. As shown in Fig. 4, the SEM image of C_{60}@PAMAM-MOF (Fig. 4A) was strikingly different from that of NC_{60}@PAMAM-MOF (Fig. 4B) in that the morphology of C_{60} changed from spherical to needle-like, and it was obvious that MOF changed the morphology of C_{60} in the direct-mixing method. Meanwhile, the topical SEM image of C_{60}@PAMAM (Fig. 4C) exhibited spherical C_{60} nanoparticles stacked together to form an irregular structure with a dendritic distribution. These results were confirmed with TEM images, as shown in Fig. 4D, E and F.

In order to further illustrate signal amplification of the tracer labels, the role and optimal amount of AuNPs in the three tracer labels were studied firstly. AuNPs with excellent conductivity are capable of binding with amino and sulfhydryl groups via strong

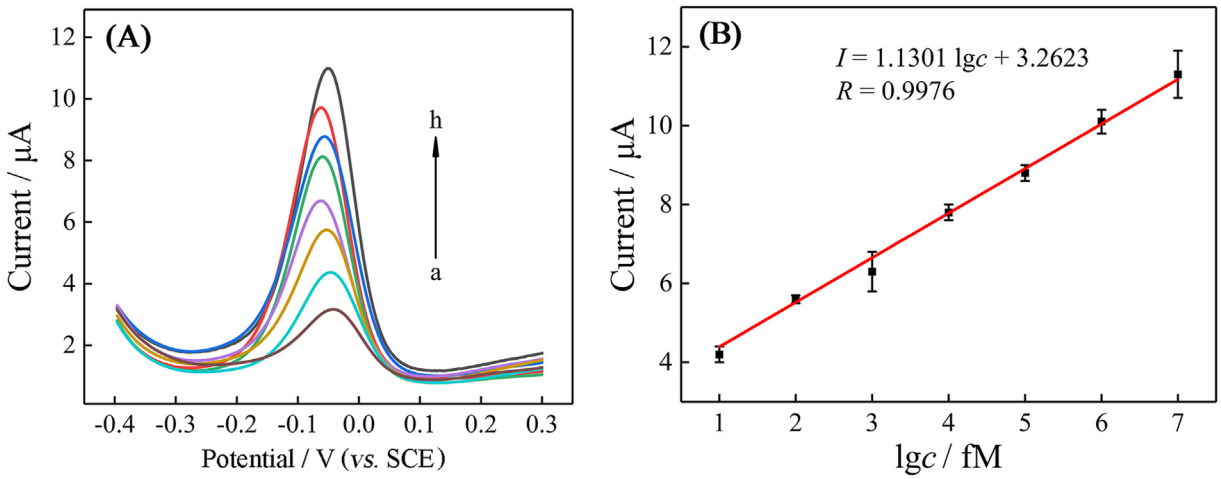

Fig. 6. (A) DPV response of biosensor for detection of miR-3675-3p with different concentrations (a→h: blank, 10 fM, 100 fM, 1 pM, 10 pM, 100 pM, 1 nM and 10 nM) in the 0.1 M PBS. (B) The calibration curve between current and concentration logarithm. The error bars represent the standard deviation of three parallel determinations.

covalent bonds and high affinity [43–48]. In this work, three nanohybrids in virtue of abundant amino groups can adsorb AuNPs via Au–N bonds, which not only enhanced electron transfer, but also immobilized SP via Au–S bonds to form tracer labels. In addition, the dosages of $HAuCl_4$ (1%) to produce different amounts of AuNPs in the three tracer labels were also investigated. As shown in Fig. S1 (see in Supplementary Material), the peak current reached a maximum at 1 mL of $HAuCl_4$, indicating that the optimal amount of AuNPs was obtained by reduction of 1 mL $HAuCl_4$ (1%) with $NaBH_4$. Accordingly, three tracer labels were hybridized with miR-3675-3p (10 nM) under optimal conditions and results were shown in Fig. 4G. Tracer label 1 (11.20 μA, curve a) and Tracer label 2 (7.59 μA, curve b) displayed higher current value than Tracer label 3 (3.90 μA, curve c), which was attributed to the synergetic reaction between MOF and C_{60} enhancing the redox activity of C_{60} to achieve signal amplification. Furthermore, the current value of Tracer label 1 was about 1.5 times higher than that of Tracer label 2, which indicated that the phase-transfer method was superior to the direct-mixing method. Consequently, with the above factors, Tracer label 1 was selected for subsequent experiment.

3.5. Optimization of experimental parameters

The concentration ratio of MOF:C_{60}. The ratio of MOF and C_{60} was critical to the signal response of the biosensor. In order to find the optimal concentration ratio, various concentration ratios (MOF:C_{60} = X:1, X = 0.25, 0.5, 1, 2, 4) were tested for detection of miR-3675-3p (1 nM). As observed from Fig. 5A, the current value arrived at the maximum and the material evenly dispersed at a ratio of 1:1. At higher ratios, the current value decreased, which was mainly due to the combination saturation of C_{60} with MOF, and excrescent MOF would hinder electron transfer. Consequently, the optimum doping concentration ratio of MOF:C_{60} was 1:1.

The pH of PBS buffer. To obtain higher sensitivity, the different pH levels (3, 5, 7, 9, 11) were investigated by DPV for detection of miR-3675-3p (10 pM). As shown in Fig. 5B, the current value gradually increased in the range of 3–7 and reached the peak at pH of 7. Under the high acidic and basic conditions, the buffer system of the human body will be broken and the structures/sequences of nucleotides will be affected [49], resulting in a decrease of current response. Therefore, pH of 7 was selected as the most suitable pH and used in the subsequent experiments.

Hybridization temperature and time. The hybridization process between the miRNA and Tracer label 1 is important for the detection of miR-3675-3p. Therefore, different temperatures (25, 30, 35, 37, 40, 45 °C) and reaction times (0.5, 1.5, 2.0, 2.5, 3.0 h) of hybridization were investigated by CV for detection of miR-3675-3p (10 nM). As depicted in Fig. 5C, the current value increased as the hybridization temperature increased and rose to peak value at 37 °C, which was also the physiological temperature of the human and can maintain miRNA activity, while high temperatures will cause denaturation of nucleic acids [50,51]. Therefore, 37 °C was selected as optimum hybridization temperature. As for hybridization time, the maximum current response was reached at 2 h in the range of 0.5 h–3 h (Fig. 5D). Thus, the optimum hybridization time was 2 h.

3.6. Performance evaluation of the miRNA biosensor

3.6.1. DPV response and calibration curve

Under the optimal experiment parameters, DPV was used to record signal response at different concentrations of miR-3675-3p in 0.1 M PBS. As shown in Fig. 6A, the miRNA biosensor displayed a good linear range from 10 fM to 10 nM, and the calibration curve was $I = 1.1301\ \lg c + 3.2623$ with a correlation coefficient of 0.9976 as illustrated in Fig. 6B (three parallel experiments were tested, n = 3). The limit of detection (LOD) as calculated with $M + 3\sigma$ (M: the average of DPV signal response; σ: the standard deviation of blank solution) was 2.99 fM [52,53]. As shown in Table 2, the proposed biosensor displayed a wider linear range and a lower LOD compared with other biosensors.

Table 2
Comparison with others proposed electrochemical biosensor for miRNA detection.

Detection method	Target	linear range	LOD	Ref.
ECL	miR-182	0.1 pM–100 pM	33 fM	[54]
ECL	miR-141	10 fM~100 pM	3.3 fM	[55]
EIS	miR-21	10 fM~100 pM	4.3 fM	[56]
CV	Let-7a	50 fM~0.9 pM	16 fM	[57]
SWV	Let-7d-5p	1 pM–10 nM	0.17 pM	[58]
SWV	miR-21	1 pM–10 nM	0.26 pM	[59]
DPV	miR-21	10 fM~100 pM	3.5 fM	[60]
DPV	miR-182	10 fM~10 pM	0.01 pM	[61]
DPV	miR-3675-3p	10 fM~10 nM	2.99 fM	This work

ECL: electrochemiluminescence; SWV: square wave voltammetry.

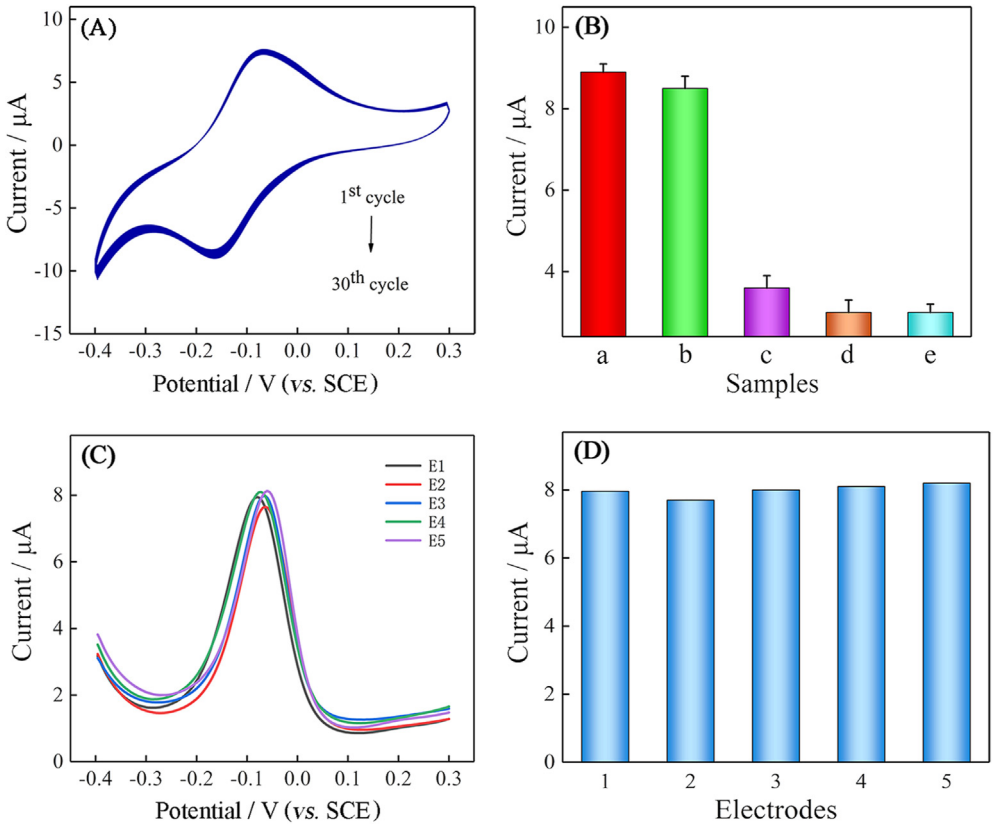

Fig. 7. (A) Stability of the biosensor with continuously scanned for 30 CV cycles in the 0.1 M PBS. (B) Specificity of the biosensor with various interfering substances (a→e: miR-3675-3p, the mixture miRNA, SBM, Let-7d-5p and blank). Error bars represented the standard deviation of three parallel values. (C) DPV responses and (D) histogram of five electrodes incubated with miR-3675-3p (10 pM) in the same batch (inter-assay).

Table 3
Detection of miR-3675-3p in human serum samples with the as-prepared biosensor.

Serum sample	Added miR-3675-3p (pM)	Found miR-3675-3p (pM)[a]	RSD (%)	Recovery (%)
S1	0.01	0.0096	3.13	96.0
S2	0.1	0.0942	2.34	94.2
S3	0.5	0.488	2.04	97.6
S4	500	518.43	5.32	103.7

[a] The mean value of measurement (n = 3).

3.6.2. *Stability, specificity and reproducibility of the designed biosensor*

Stability was a pivotal parameter for the designed biosensor, which was evaluated with continuous CV scanning and tested after long-term storage test at 4 °C. As depicted in Fig. 7A, the electrode with 10 nM miR-3675-3p was continuously scanned for 30 cycles in 0.1 M PBS (pH = 7.4), and the current remained at 93.73% of the original value. In addition, the biosensor was incubated with miR-3675-3p (1 nM) and stored at 4 °C for 14 days, and the current remained at 97.92% and 82.11% of the original value after 7 days and 14 days, respectively. As shown in Table S2 (see in Supplementary Material), the designed biosensor exhibited acceptable stability compared with other literatures.

Specificity and reproducibility are also important for a biosensor. Specificity of the biosensor was assessed by the target miRNA (100 pM), a miRNA mixture of miR-3675-3p (100 pM) and Let-7d-5p (100 pM) (v/v = 2:1), a single base mismatch sequence (SBM, 100 pM), another miRNA (Let-7d-5p, 100 pM) and a blank solution. As depicted in Fig. 7B, the signal of target miRNA was significantly higher than that of other samples, and there was no significant difference between Let-7d-5p and the blank. Additionally, the reproducibility was evaluated by measuring five electrodes incubated with miR-3675-3p (10 pM) in the same batch (inter-assay) and in the different batches (intra-assay). As depicted in Fig. 7C and D, the current values are relatively close among the electrodes, and the relative standard deviation (RSD) of inter-assay was 2.35%. Moreover, the results of intra-assay were provided in Fig. S2 (see in Supplementary Material) with an RSD of 3.05%. These results indicated outstanding specificity and excellent reproducibility of the proposed biosensor.

3.7. *Detection of clinical serum samples*

To assess the clinical utility of the designed biosensor for detection of miR-3675-3p, a recovery test was performed in the standard addition method. Healthy human serum samples were diluted 50-fold with DEPC water and were added into miR-3675-3p to prepare standard solution with various concentrations (10 fM, 100 fM, 500 fM and 500 pM). Recovery ranged from 94.2% to 103.7% and RSD from 2.04% to 5.32% as shown in Table 3, indicating

acceptable recovery of the biosensor. Besides, the clinical serum samples of healthy donors and IPF patients were assayed to verify the clinical practice of the biosensor further. As shown in Fig. S3 (see in Supplementary Material), the serum samples from IPF patient presented higher the current responses than that of the healthy donors, indicating the emergence of a hopeful detection method for IPF diagnosis.

In addition, a qRT-PCR experiment was employed to further explore the feasibility of clinical application of the miRNA biosensor and was described in Supplementary Material. First of all, the standard curve was established and showed a narrower linear range (from 16 nM to 2 μM, Figs. S4A and B) compared with our biosensor (from 10 fM to 10 nM). Secondly, the extracted total RNA samples were extracted from the serum of five healthy donors, and were subjected to detection with qRT-PCR and the biosensor. As shown in Fig. S4C, the high Ct value was attributed to the fact that the concentration of miR-3675-3p in serum samples of healthy people was lower than the detection limit of qRT-PCR, so it is difficult to carry out quantitative determination. However, the as-proposed biosensor exhibited satisfactory results as shown in Fig. S4D. In conclusion, the biosensor showed a wider linear range and lower LOD than that of qRT-PCR, and had great potential in detection of miR-3675-3p.

4. Conclusions

In summary, the new nanohybrid of C_{60}@PAMAM-MOF was successfully prepared and served as redox nanoprobe and nanocarrier for the construction of an electrochemical miRNA biosensor to detect miR-3675-3p. It is of note that C_{60}@PAMAM-MOF has displayed prominent redox activity and good conductivity, attributing to the synergistic effect and the active electron transfer between MOF and C_{60}. Furthermore, C_{60}@PAMAM-MOF coupled with AB and Au@PtNPs to amplify electrochemical signals, which improved the sensitivity of the biosensor and lowered the detection limit to femtomolar level. The proposed biosensor exhibited outstanding reproducibility and specificity. More significantly, it showed good recovery (from 94.2% to 103.7%) in the spiked serum and satisfactory results in the detection of healthy serum samples, which opened up new avenues for detection of miR-3675-3p and provided a promising detection platform for other miRNA biomarkers and biological samples.

CRediT authorship contribution statement

Jianli Zuo: Conceptualization, Methodology, Formal analysis, Writing - original draft, Visualization. **Yonghua Yuan:** Conceptualization, Investigation, Resources, Funding acquisition. **Min Zhao:** Software, Supervision. **Jie Wang:** Software. **Yuhan Chen:** Investigation, Visualization. **Qiqi Zhu:** Investigation, Software. **Lijuan Bai:** Methodology, Resources, Writing - review & editing, Funding acquisition.

Declaration of competing interest

The authors declare that they have no known competing financial interests or personal relationships that could have appeared to influence the work reported in this paper.

Acknowledgements

This work is supported by National Natural Science Foundation of China (82072378, 81570010), Chongqing Talent Program, China (2020), Ba Yu Scholar Program, China (YS2019020), Funds for High Level Young Science and Technology Talent Cultivation Plan in Chongqing Medical University, China (2019), Discipline Talent Training Program of College of Pharmacy in Chongqing Medical University, China (YXY2019XSGG4) and the Third Batch of Young Backbone Teachers Funding Program in Colleges and Universities of Chongqing, China (2016).

Appendix A. Supplementary data

Supplementary data to this article can be found online at https://doi.org/10.1016/j.aca.2020.10.017.

References

[1] D.J. Lederer, F.J. Martinez, Idiopathic pulmonary fibrosis, N. Engl. J. Med. 378 (2018) 1811–1823.
[2] F.J. Martinez, H.R. Collard, A. Pardo, G. Raghu, L. Richeldi, M. Selman, J.J. Swigris, H. Taniguchi, A.U. Wells, Idiopathic pulmonary fibrosis, Nat Rev Dis Primers 3 (2017) 17074.
[3] G. Raghu, M. Remy-Jardin, J.L. Myers, L. Richeldi, C.J. Ryerson, D.J. Lederer, J. Behr, V. Cottin, S.K. Danoff, F. Morell, K.R. Flaherty, A. Wells, F.J. Martinez, A. Azuma, T.J. Bice, D. Bouros, K.K. Brown, H.R. Collard, A. Duggal, L. Galvin, Y. Inoue, R.G. Jenkins, T. Johkoh, E.A. Kazerooni, M. Kitaichi, S.L. Knight, G. Mansour, A.G. Nicholson, S.N.J. Pipavath, I. Buendia-Roldan, M. Selman, W.D. Travis, S. Walsh, K.C. Wilson, E.R.S.J.R.S, S. American Thoracic Society, Latin American thoracic, diagnosis of idiopathic pulmonary fibrosis. An official ATS/ERS/JRS/ALAT clinical practice guideline, Am. J. Respir. Crit. Care Med. 198 (2018) e44–e68.
[4] F.J. Martinez, A. Chisholm, H.R. Collard, K.R. Flaherty, J. Myers, G. Raghu, S.L.F. Walsh, E.S. White, L. Richeldi, The diagnosis of idiopathic pulmonary fibrosis: current and future approaches, Lancet Resp. Med. 5 (2017) 61–71.
[5] M. Romagnoli, T.V. Colby, J.-P. Berthet, A.S. Gamez, J.-P. Mallet, I. Serre, A. Cancellieri, A. Cavazza, L. Solovei, A. Dell'Amore, G. Dolci, A. Guerrieri, P. Reynaud, S. Bommart, M. Zompatori, G. Dalpiaz, S. Nava, R. Trisonlini, C.M. Suehs, I. Vachier, N. Molinari, A. Bourdin, Poor concordance between sequential transbronchial lung cryobiopsy and surgical lung biopsy in the diagnosis of diffuse interstitial lung diseases, Am. J. Respir. Crit. Care Med. 199 (2019) 1249–1256.
[6] C. Miao, Y. Xiong, G. Zhang, J. Chang, MicroRNAs in idiopathic pulmonary fibrosis, new research progress and their pathophysiological implication, Exp. Lung Res. 44 (2018) 178–190.
[7] D. Pattarayan, R.K. Thimmulappa, V. Ravikumar, S. Rajasekaran, Diagnostic potential of extracellular MicroRNA in respiratory diseases, Clin. Rev. Allergy Immunol. 54 (2016) 480–492.
[8] P. Li, J. Li, T. Chen, H. Wang, H. Chu, J. Chang, W. Zang, Y. Wang, Y. Ma, Y. Du, G. Zhao, G. Zhang, Expression analysis of serum microRNAs in idiopathic pulmonary fibrosis, Int. J. Mol. Med. 33 (2014) 1554–1562.
[9] T. Ouyang, Z. Liu, Z. Han, Q. Ge, MicroRNA detection specificity: recent advances and future perspective, Anal. Chem. 91 (2019) 3179–3186.
[10] X. Sun, Y. Wang, L. Zhang, S. Liu, M. Zhang, J. Wang, B. Ning, Y. Peng, J. He, Y. Hu, Z. Gao, A CRISPR-Cas9 triggered two-step isothermal amplification method for E. coli O157:H7 Detection Based on a metal-organic framework platform, Anal. Chem. 92 (2020) 3032–3041.
[11] S. Liu, J. Bai, Y. Huo, B. Ning, Y. Peng, S. Li, D. Han, W. Kang, Z. Gao, A zirconium-porphyrin MOF-based ratiometric fluorescent biosensor for rapid and ultrasensitive detection of chloramphenicol, Biosens. Bioelectron. 149 (2020) 111801.
[12] Y. Wang, J. Wang, D. Wei, M. Li, A "MOF-protective-pyrolysis" strategy for the preparation of Fe-N-C catalysts and the role of Fe, N, and C in the oxygen reduction reaction in acidic medium, ACS Appl. Mater. Interfaces 11 (2019) 35755–35763.
[13] H. Li, K. Wang, Y. Sun, C.T. Lollar, J. Li, H.-C. Zhou, Recent advances in gas storage and separation using metal-organic frameworks, Mater. Today 21 (2018) 108–121.
[14] Y. Wang, J. Yan, N. Wen, H. Xiong, S. Cai, Q. He, Y. Hu, D. Peng, Z. Liu, Y. Liu, Metal-organic frameworks for stimuli-responsive drug delivery, Biomaterials 230 (2020) 119619.
[15] J. Fu, X. Wang, T. Wang, J. Zhang, S. Guo, S. Wu, F. Zhu, Covalent functionalization of graphene oxide with a presynthesized metal-organic framework enables a highly stable electrochemical sensing, ACS Appl. Mater. Interfaces 11 (2019) 33238–33244.
[16] F. Cai, Q. Wang, X. Chen, W. Qiu, F. Zhan, F. Gao, Q. Wang, Selective binding of Pb^{2+} with manganese-terephthalic acid MOF/SWCNTs: theoretical modeling, experimental study and electroanalytical application, Biosens. Bioelectron. 98 (2017) 310–316.
[17] B. Hatamluyi, A. Hashemzadeh, M. Darroudi, A novel molecularly imprinted polymer decorated by CQDs@HBNNS nanocomposite and UiO-66-NH_2 for ultra-selective electrochemical sensing of Oxaliplatin in biological samples, Sensor. Actuator. B Chem. 307 (2020) 127164.
[18] H. You, L. Bai, Y. Yuan, J. Zhou, Y. Bai, Z. Mu, An amperometric aptasensor for ultrasensitive detection of sulfadimethoxine based on exonuclease-assisted target recycling and new signal tracer for amplification, Biosens.

Bioelectron. 117 (2018) 706–712.
[19] Y. Chen, S. Guo, M. Zhao, P. Zhang, Z. Xin, J. Tao, L. Bai, Amperometric DNA biosensor for *Mycobacterium tuberculosis* detection using flower-like carbon nanotubes-polyaniline nanohybrid and enzyme-assisted signal amplification strategy, Biosens. Bioelectron. 119 (2018) 215–220.
[20] J. Han, Y. Zhuo, Y.-Q. Chai, Y. Xiang, R. Yuan, A new type of redox nanoprobe: C_{60}-based nanomaterial and its application in electrochemical immunoassay for doping detection, Anal. Chem. 87 (2015) 1669–1675.
[21] L. Bai, Y. Chen, Y. Bai, Y. Chen, J. Zhou, A. Huang, Fullerene-doped polyaniline as new redox nanoprobe and catalyst in electrochemical aptasensor for ultrasensitive detection of *Mycobacterium tuberculosis* MPT64 antigen in human serum, Biomaterials 133 (2017) 11–19.
[22] Y. Chen, X. Liu, S. Guo, J. Cao, J. Zhou, J. Zuo, L. Bai, A sandwich-type electrochemical aptasensor for *Mycobacterium tuberculosis* MPT64 antigen detection using C_{60}NPs decorated N-CNTs/GO nanocomposite coupled with conductive PEI-functionalized metal-organic framework, Biomaterials 216 (2019) 119253.
[23] S. Goswami, D. Ray, K.-I. Otake, C.-W. Kung, S.J. Garibay, T. Islamoglu, A. Atilgan, Y. Cui, C.J. Cramer, O.K. Farha, J.T. Hupp, A porous, electrically conductive Hexa-Zirconium (IV) metal-organic framework, Chem. Sci. 9 (2018) 4477–4482.
[24] H. Ibrahim, M. Ibrahim, Y. Temerk, A novel megestrol acetate electrochemical sensor based on conducting functionalized acetylene black-CeO_2NPs nanohybrids decorated glassy carbon microspheres, Talanta 200 (2019) 324–332.
[25] H.-L. Shuai, K.-J. Huang, Y.-X. Chen, A layered tungsten disulfide/acetylene black composite based DNA biosensing platform coupled with hybridization chain reaction for signal amplification, J. Mat. Chem. B 4 (2016) 1186–1196.
[26] L. Jiao, Z. Mu, C. Zhu, Q. Wei, H. Li, D. Du, Y. Lin, Graphene loaded bimetallic Au@Pt nanodendrites enhancing ultrasensitive electrochemical immunoassay of AFP, Sensor. Actuator. B Chem. 231 (2016) 513–519.
[27] Y. Yu, C. Yu, Y. Niu, J. Chen, Y. Zhao, Y. Zhang, R. Gao, J. He, Target triggered cleavage effect of DNAzyme: relying on Pd-Pt alloys functionalized Fe-MOFs for amplified detection of Pb^{2+}, Biosens. Bioelectron. 101 (2018) 297–303.
[28] S. Tang, H. Shen, Y. Hao, Z. Huang, Y. Tao, Y. Peng, Y. Guo, G. Xie, W. Feng, A novel cytosensor based on Pt@Ag nanoflowers and AuNPs/Acetylene black for ultrasensitive and highly specific detection of Circulating Tumor Cells, Biosens. Bioelectron. 104 (2018) 72–78.
[29] L. Li, Y. Yuan, Y. Chen, P. Zhang, Y. Bai, L. Bai, Aptamer based voltammetric biosensor for *Mycobacterium tuberculosis* antigen *ESAT-6* using a nanohybrid material composed of reduced graphene oxide and a metal-organic framework, Microchim. Acta 185 (2018) 370–379.
[30] M. Hu, Y. Wang, J. Yang, Y. Sun, G. Xing, R. Deng, X. Hu, G. Zhang, Competitive electrochemical immunosensor for maduramicin detection by multiple signal amplification strategy via hemin@Fe-MIL-88NH_2/AuPt, Biosens. Bioelectron. 142 (2019) 111554.
[31] D.M. Guldi, G.M. Rahman, V. Sgobba, C. Ehli, Multifunctional molecular carbon materials—from fullerenes to carbon nanotubes, Chem. Soc. Rev. 35 (2006) 471–487.
[32] M.-H. Pham, G.-T. Vuong, A.-T. Vu, T.-O. Do, Novel route to size-controlled Fe-MIL-88B-NH_2 metal-organic framework nanocrystals, Langmuir 27 (2011) 15261–15267.
[33] Y. Fu, D. Sun, Y. Chen, R. Huang, Z. Ding, X. Fu, Z. Li, An amine-functionalized titanium metal-organic framework photocatalyst with visible-light-induced activity for CO_2 reduction, Angew. Chem. Int. Ed. 51 (2012) 3364–3367.
[34] A. Yurduşen, Y. Yürüm, A controlled synthesis strategy to enhance the CO_2 adsorption capacity of MIL-88B type MOF crystallites by the crucial role of narrow micropores, Ind. Eng. Chem. Res. 58 (2019) 14058–14072.
[35] Y. Zhang, F. Wang, H. Zhang, H. Wang, Y. Liu, Multivalency interface and g-C_3N_4 coated liquid metal nanoprobe signal amplification for sensitive electrogenerated chemiluminescence detection of exosomes and their surface proteins, Anal. Chem. 91 (2019) 12100–12107.
[36] H. Jin, R. Gui, X. Gao, Y. Sun, An amplified label-free electrochemical aptasensor of γ-interferon based on target-induced DNA strand transform of hairpin-to-linear conformation enabling simultaneous capture of redox probe and target, Biosens. Bioelectron. 145 (2019) 111732.
[37] Y. Li, C. Yu, B. Yang, Z. Liu, P. Xia, Q. Wang, Target-catalyzed hairpin assembly and metal-organic frameworks mediated nonenzymatic co-reaction for multiple signal amplification detection of miR-122 in human serum, Biosens. Bioelectron. 102 (2018) 307–315.
[38] H. Chen, Q. Lu, J. Liao, R. Yuan, S. Chen, Anodic electrogenerated chemiluminescence behavior and the choline biosensing application of blue emitting conjugated polymer dots, Chem. Commun. 52 (2016) 7276–7279.
[39] X. Chang, P.J. Vikesland, UV-vis spectroscopic properties of nC_{60} produced via extended mixing, Environ. Sci. Technol. 45 (2011) 9967–9974.
[40] B. Thirumalraj, S. Palanisamy, S.-M. Chen, C.-Y. Yang, P. Periakaruppan, B.-S. Lou, Direct electrochemistry of glucose oxidase and sensing of glucose at a glassy carbon electrode modified with a reduced graphene oxide/fullerene-C_{60} composite, RSC Adv. 5 (2015) 77651–77657.
[41] H. Dong, F. Zou, X. Hu, H. Zhu, K. Koh, H. Chen, Analyte induced AuNPs aggregation enhanced surface plasmon resonance for sensitive detection of paraquat, Biosens. Bioelectron. 117 (2018) 605–612.
[42] K. Kadan-Jamal, M. Sophocleous, A. Jog, D. Desagani, O. Teig-Sussholz, J. Georgiou, A. Avni, Y. Shacham-Diamand, Electrical Impedance Spectroscopy of plant cells in aqueous biological buffer solutions and their modelling using a unified electrical equivalent circuit over a wide frequency range: 4Hz to 20, GHz 168 (2020) 112485.
[43] R. Rice, N. Pontikos, R. McCreery, Quantitative correlations of heterogeneous electron-transfer kinetics with surface properties of glassy carbon electrodes, J. Am. Chem. Soc. 112 (1990) 4617–4622.
[44] A. Shelke, A. Lokhande, R. Pujari, C. Lokhande, Modification in supercapacitive behavior of CoO-rGO composite thin film from exposure to ferri/ferrocyanide redox active couple, J. Colloid Interface Sci. 522 (2018) 111–119.
[45] L. Bai, Y. Chai, X. Pu, R. Yuan, A signal-on electrochemical aptasensor for ultrasensitive detection of endotoxin using three-way DNA junction-aided enzymatic recycling and graphene nanohybrid for amplification, Nanoscale 6 (2014) 2902–2908.
[46] Y. Zhang, J. Song, Q. Pan, X. Zhang, W. Shao, X. Zhang, C. Quan, J. Li, An Au@NH_2-MIL-125(Ti)-based multifunctional platform for colorimetric detections of biomolecules and Hg^{2+}, J. Mat. Chem. B 8 (2020) 114–124.
[47] H. Shao, H. Lin, Z. Guo, J. Lu, Y. Jia, M. Ye, F. Su, L. Niu, W. Kang, S. Wang, Y. Hu, Y. Huang, A multiple signal amplification sandwich-type SERS biosensor for femtomolar detection of miRNA, Biosens. Bioelectron. 143 (2019) 111616.
[48] K.C. Grabar, R.G. Freeman, M.B. Hommer, M.J. Natan, Preparation and characterization of Au colloid monolayers, Anal. Chem. 67 (1995) 735–743.
[49] A. Sabahi, R. Salahandish, A. Ghaffarinejad, E. Omidinia, Electrochemical nanogenosensor for highly sensitive detection of miR-21 biomarker based on SWCNT-grafted dendritic Au nanostructure for early detection of prostate cancer, Talanta 209 (2020) 120595.
[50] L. Tian, J. Qi, X. Ma, X. Wang, C. Yao, W. Song, Y. Wang, A Facile DNA Strand Displacement Reaction Sensing Strategy of Electrochemical Biosensor Based on N-Carboxymethyl Chitosan/molybdenum Carbide Nanocomposite for microRNA-21 Detection, vol. 122, 2018, pp. 43–50.
[51] T. Meng, H. Jia, S. An, H. Wang, X. Yang, Y. Zhang, Pd nanoparticles-DNA layered nanoreticulation biosensor based on target catalytic hairpin assembly for ultrasensitive and selective, biosensing of microRNA-21 323 (2018) 128621.
[52] P. Zhang, J. Jiang, R. Yuan, Y. Zhuo, Y. Chai, Highly ordered and field-free 3D DNA nanostructure: the next generation of DNA nanomachine for rapid single-step sensing, J. Am. Chem. Soc. 140 (2018) 9361–9364.
[53] L. Liu, Y. Wei, S. Jiao, S. Zhu, X. Liu, A novel label-free strategy for the ultrasensitive miRNA-182 detection based on MoS_2/Ti_3C_2 nanohybrids, Biosens. Bioelectron. 137 (2019) 45–51.
[54] H.-Y. Zhu, S.-N. Ding, Dual-signal-amplified electrochemiluminescence biosensor for microRNA detection by coupling cyclic enzyme with CdTe QDs aggregate as luminophor, Biosens. Bioelectron. 134 (2019) 109–116.
[55] Z. Xu, L. Liao, Y. Chai, H. Wang, R. Yuan, Ultrasensitive electrochemiluminescence biosensor for MicroRNA detection by 3D DNA walking machine based target conversion and distance-controllable signal quenching and enhancing, Anal. Chem. 89 (2017) 8282–8287.
[56] K. Zhang, N. Zhang, L. Zhang, H. Wang, H. Shi, Q. Liu, Label-free impedimetric sensing platform for microRNA-21 based on ZrO_2-reduced graphene oxide nanohybrids coupled with catalytic hairpin assembly amplification, RSC Adv. 8 (2018) 16146–16151.
[57] Y. Li, R. Tian, X. Zheng, R. Huang, Amplified electrochemical detection of nucleic acid hybridization via selective preconcentration of unmodified gold nanoparticles, Anal. Chim. Acta 934 (2016) 59–65.
[58] Y. Tao, D. Yin, M. Jin, J. Fang, T. Dai, Y. Li, Y. Li, Q. Pu, G. Xie, Double-loop hairpin probe and doxorubicin-loaded gold nanoparticles for the ultrasensitive electrochemical sensing of microRNA, Biosens. Bioelectron. 96 (2017) 99–105.
[59] D. Zhu, W. Liu, D. Zhao, Q. Hao, J. Li, J. Huang, J. Shi, J. Chao, S. Su, L. Wang, Label-free electrochemical sensing platform for MicroRNA-21 detection using thionine and gold nanoparticles Co-functionalized MoS_2 nanosheet, ACS Appl. Mater. Interfaces 9 (2017) 35597–35603.
[60] Z. Chen, Y. Xie, W. Huang, C. Qin, A. Yu, G. Lai, Exonuclease-assisted target recycling for ultrasensitive electrochemical detection of microRNA at vertically aligned carbon nanotubes, Nanoscale 11 (2019) 11262–11269.
[61] J. Chang, H. Li, F. Li, Diffusivity and intercalation of electroactive dyes-mediated truly ratiometric homogeneous electrochemical strategy for highly sensitive biosensing, Chem. Commun. 55 (2019) 10603–10606.